Small-signal stability analysis and control system design of a meshed multi-terminal high-voltage direct current grid with a current flow controller

Deng, Na; Wang, Puyu; Zhang, Xiao-Ping

DOI:
10.1080/15325008.2016.1153750

Electric Power Components and Systems

ISSN: 1532-5008 (Print) 1532-5016 (Online) Journal homepage: http://www.tandfonline.com/loi/uemp20

Small-signal Stability Analysis and Control System Design of a Meshed Multi-terminal High-Voltage Direct Current Grid with a Current Flow Controller

Na Deng, Puyu Wang & Xiao-Ping Zhang

To cite this article: Na Deng, Puyu Wang & Xiao-Ping Zhang (2016): Small-signal Stability Analysis and Control System Design of a Meshed Multi-terminal High-Voltage Direct Current Grid with a Current Flow Controller, Electric Power Components and Systems

To link to this article: http://dx.doi.org/10.1080/15325008.2016.1153750

Published online: 21 May 2016.

Electric Power Components and Systems, 00(00):1–12, 2016

ISSN: 1532-5008 print / 1532-5016 online
DOI: 10.1080/15325008.2016.1153750

Taylor & Francis
Taylor & Francis Group

Small-signal Stability Analysis and Control System Design of a Meshed Multi-terminal High-Voltage Direct Current Grid with a Current Flow Controller

Na Deng, Puyu Wang[2] and Xiao-Ping Zhang[2]
[1]ABB Sifang Power System Co., Ltd, Shunyi District, Beijing, China
[2]Department of Electronic, Electrical and Systems Engineering, School of Engineering, University of Birmingham, Edgbaston, Birmingham, UK

CONTENTS

Abstract—A DC current flow controller can provide branch current control in a meshed multi-terminal high-voltage direct current (HVDC) grid. However, the introduction of a DC current flow controller may affect the stability of the multi-terminal HVDC. Hence, the dynamic characteristics of the multi-terminal HVDC with the DC current flow controller should be investigated. This article focuses on small-signal stability analysis of a current flow controller-equipped meshed three-terminal HVDC system. A small-signal model for the multi-terminal HVDC with the DC current flow controller is established. Based on the stability analysis of the small-signal model, a control system is designed for the DC current flow controller, fulfilling the system stability requirement. Finally, non-linear dynamic simulations on the real-time digital simulator are conducted, and simulation results are compared with a theoretical model to validate the proposed controller for the DC current flow controller. In addition, dynamic impacts of the DC current flow controller on the meshed multi-terminal HVDC grid are discussed.

Keywords: current flow controller, controller design, meshed multi-terminal high-voltage direct current, small-signal dynamic modeling, stability analysis, real-time digital simulator

Received 21 February 2015; accepted 20 January 2016

Address correspondence to Dr. Xiao-Ping Zhang, Department of Electronic, Electrical and Systems Engineering, School of Engineering, University of Birmingham, Edgbaston, Birmingham, B15 2TT, United Kingdom. E-mail: x.p.zhang@bham.ac.uk
Color versions of one or more of the figures in the article can be found online at www.tandfonline.com/uemp.

1. INTRODUCTION

HVDC grids have become increasingly popular due to their advantages over HVAC grids for long distance, underwater, and underground transmission applications, as well as applications in offshore wind farms and urban transmission systems [1–3]. Recently, multi-terminal HVDC (MTDC) grids have attracted more attention on the interconnection of power systems between different countries or regions [4] and the development of offshore wind farms [5, 6].

In terms of building MTDC systems, voltage source converter (VSC) technologies are preferable over line-commutated converter (LCC) technologies, and the use of meshed structures is preferable over the use of radial structures. In the first case, VSC HVDC can regulate the active and reactive power flows independently [7]. In the second case, meshed structures can offer better DC cable utilization and lower capital costs as well as higher reliability and flexibility compared with radial structures [8–10].

However, one deficiency of a meshed grid is that the branch currents cannot be fully controlled through converter stations. Three types of control devices capable of DC power flow control have been proposed to date [11–23]: variable resistor, DC transformer, and series voltage source. Two methods of providing DC power flow control by inserting variable resistance into a DC line were presented in [11, 12], in which the DC branch current is well controlled by switching on and off the variable resistance of the device. However, the power loss due to the switch-in resistance is an undesirable outcome. The second type of DC power flow control method is by means of a DC-DC transformer. Several different topologies of DC-DC transformers were proposed [11, 13, 14]; however, the DC-DC transformers have to withstand high voltage and power, which results in high construction cost and losses. The third type of DC power flow method is inserting an equivalent voltage source into a DC line to regulate the power/current flow. A variable voltage source based on a thyristor control method for regulating the power flow in meshed MTDC grid was proposed in [15]. Two patented methods with several different circuits for the variable voltage source were applied in [16, 17]; comparisons regarding these methods were carried out in [12]. In comparison with an inserted variable resistor and a DC-DC transformer, a variable voltage source has a much smaller power rating and losses, requires a lower voltage rating, and can easily be implemented.

Among the existing approaches of adopting variable voltage source for the DC power flow control, most of them required the connection with an external AC source to export/import power from/to the DC grid [18–20]. Only two DC power flow controller (PFC) topologies avoided the use of an external AC or DC source [21–23]. This type of current flow controller (CFC) or PFC has the benefits of simple circuit topology and no external AC sources. In [22], the CFC was very briefly introduced and no control strategies were presented. In [23], the steady-state model of the CFC was studied. However, the steady-state model may not be sufficient in explicitly revealing the system dynamic performance and system stability. There may be a risk that the original HVDC system may become unstable with the application of the CFC. Hence, it is important to establish a small-signal model for the system with the installation of a CFC. The small-signal model is generally used for non-linear system analysis. By developing the small-signal model, the system eigenvalues and transfer functions (TFs) can be derived, and thus, the system stability and dynamic performance can be evaluated. Furthermore, based on the small-signal model, the control system parameters can be designed to achieve satisfactory dynamic responses.

Based on these reasons, this article is focused on the development of the small-signal stability and control system design of a meshed three-terminal (3-T) HVDC system with the installation of a CFC. There are two major contributions of the proposed system. (1) The small-signal model of the system is developed, which includes (a) the dynamics of the CFC, (b) the dynamics of the voltage and power controllers of the CFC, and (c) the dynamics of the meshed DC grid. (2) Based on the small-signal modeling, a control system is designed for the DC CFC to satisfy both steady-state and dynamic operating requirements. To validate the small-signal stability model and the controller designed for the DC CFC, simulations are carried out on a real-time digital simulator (RTDS) and compared with the theoretical modeling results. Finally, analysis of the impact of DC devices on meshed HVDC grids is provided.

The rest of this article is arranged as follows. Section 2 describes the configuration of a meshed 3-T modular multilevel converter (MMC) HVDC system and explains the needs for a CFC. In Section 3, the operating principle of the CFC is explained. In Section 4, the small-signal dynamic model for the 3-T HVDC network with the CFC is derived. Based on the small-signal dynamic model, the system analysis and control system design are conducted in Section 5. Simulation studies are presented in Section 6 followed by conclusions in Section 7.

2. MESHED 3-T MMC HVDC SYSTEM

2.1. System Configuration

The single-line diagram of a meshed 3-T MMC HVDC system with the installation of a CFC is shown in Figure 1. There are three terminals, namely T_1, T_2, and T_3. The AC systems of the three terminals have the same structures and parameters. The converters use an MMC structure. The DC system is a ±160-kV, 640-MVA meshed system.

2.2. Control Strategy of the MMCs

For the MMCs in Figure 1, the *DQ* decoupled control is applied. For the MMCs at T_1 and T_2, the control objectives are to maintain constant active power and reactive power, while for the MMC at T_3, the control objective is to maintain the DC voltage and reactive power.

The MMCs can regulate the overall power at the converter terminal, but they cannot regulate the DC current on each branch when there are branches in parallel from the same station. Therefore, it is common that the transmission lines in parallel work under unbalanced conditions, with one carrying larger current than the others. Under extreme conditions, some

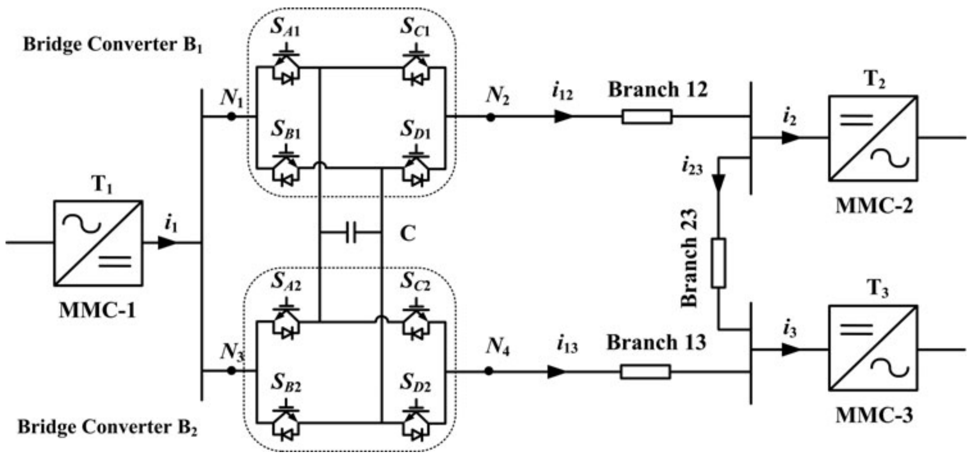

FIGURE 1. Meshed 3-T MMC HVDC grid with the installation of a CFC.

lines may operate close to their maximum current limits or are even overloaded.

To prevent either transmission line from overloading, there are several options, such as increasing the delivery capability for all transmission lines or decreasing the transmission level for the whole system. However, both decisions will greatly reduce the efficiency of the HVDC system and increase its operational cost. For these reasons, it is worth employing additional devices to regulate the branch current.

Power flow control in meshed AC grids is a traditional issue. It can be generally solved by utilizing additional series Flexible AC Transmission Systems (FACTS) devices or HVDC devices. FACTS devices can adjust the overall power flow by injecting equivalent impedance to AC lines [24]. In addition, HVDC systems can be used to control voltages and power flows in meshed AC grids [25]. Similarly, an additional power electronic-based device can be adopted to control the branch currents in a meshed DC grid. As the purpose of this power electronic device is to control the branch currents, it is also called a CFC.

3. CFC

A power electronics-based CFC is installed across branch 12 and branch 13. It consists of two DC-DC bridge converters sharing a same capacitor, which provides a channel for power exchanges between two bridge converters. By applying appropriate switching patterns to this CFC, the branch currents can be effectively controlled.

3.1. Control Strategy

The basic control strategy adopted for the CFC mimics the classical control strategy for a point-to-point VSC HVDC system. In a point-to-point VSC HVDC system, one terminal applies the constant active power control to regulate the amount and direction of the power/current through the DC system, while the other terminal employs the DC voltage control to maintain DC voltage to ensure the power balance between two terminals. A similar methodology is employed for the CFC. Upper bridge converter B_1 is assigned to regulate the current in branch 12, which is similar to active power control, while lower bridge converter B_2 is assigned to regulate the voltage across common capacitor C, which is similar to DC voltage control. In this way, the power exchange between branches 12 and 13 is realized.

3.2. Firing Signal Generation

As depicted in Figure 1, all switches are made of the combinations of insulated-gate bipolar transistors (IGBTs) and anti-parallel diodes. All switches are controlled independently through constant-frequency (CF) pulse-width modulation (PWM) signals. However, in Figure 1, some switches are connected in parallel, such as switch pairs S_{A1}/S_{A2} and S_{B1}/S_{B2}. These switch pairs need to be controlled simultaneously and share the same firing signals to make the voltage on the common capacitor build up properly.

PWM signals are produced through comparisons between different control signals and a common sawtooth wave that varies between 0 and 1 at 2 kHz. In this way, PWM signals for all switches are generated. The duty cycles of the PWM signals are defined in Table 1.

The duty cycles of these switches are triggered in a complementary way and have a fixed relationship:

$$d_a + d_b = 1, \quad d_{c1} + d_{d1} = 1, \quad d_{c2} + d_{d2} = 1. \tag{1}$$

Switches	Duty cycles	Switches	Duty cycles
S_{A1}/S_{A2}	d_a	S_{B1}/S_{B2}	d_b
S_{C1}	d_{c1}	S_{C2}	d_{c2}
S_{D1}	d_{d1}	S_{D2}	d_{d2}

TABLE 1. Duty cycles of the PWM signals for the switches in the CFC

3.2. Switching Sequence of Bridge Converters

As aforementioned, the CFC consists of two bridge converters, B_1 and B_2. Each bridge converter has four switches. According to different combinations of these four switches, both bridge converters have four modes per switching cycle, as summarized in Table 2. These four switch modes make up the switching sequences for both bridge converters. a_i is the duty cycle of switch mode i ($i = 1, \ldots, 4$) for B_1; b_j is the duty cycle of switch mode j ($j = 1, \ldots, 4$) for B_2. In addition, e_{12} is the voltage across N_1 and N_2 in Figure 1, while e_{13} is the voltage across N_3 and N_4. i_{cfc1} is the current flowing from B_1 through CFC capacitor C, and i_{cfc2} is the current from B_2 through C. u_c is the voltage across C. i_{12} is the current in branch 12, while i_{13} is the current in branch 13.

The switch modes of B_1 and B_2 are similar; therefore, only the switch modes of B_1 are later clarified. In mode 1, when S_{A1} and S_{C1} are closed, as shown in Figure 1, the common capacitor is not connected into branch 12; thus, in this mode, both e_{12} and i_{cfc1} are zero. Similarly, in mode 4, e_{12} and i_{cfc1} are also zero as the capacitor is bypassed. In mode 2, when S_{A1} and S_{D1} are switched on, the capacitor is positively connected into branch 12. Therefore, in this mode, i_{cfc1} equals i_{12} and e_{12} equals u_c. In mode 3, when S_{B1} and S_{C1} are switched on, the capacitor is negatively connected into branch 12. In this mode, the capacitor is discharged by i_{12}; therefore e_{12} equals $-u_c$. Based on the definitions of duty cycles in Table 2 and the relationships of duty ratios in Eq. (1), the following equations for the duty cycles of B_1 can be derived:

$$a_1 = \min\{d_{c1}, d_a\}, \quad a_2 = \max\{d_a - d_{c1}, 0\}, \tag{2a}$$

$$a_3 = \max\{d_{c1} - d_a, 0\}, \quad a_4 = 1 - \max\{d_a, d_{c1}\}. \tag{2b}$$

Similarly, the equations for the duty cycles of B_2 are given in Eq. (3):

$$b_1 = \min\{d_{c2}, d_a\}, \quad b_2 = \max\{d_a - d_{c2}, 0\}, \tag{3a}$$

$$b_3 = \max\{d_{c2} - d_a, 0\}, \quad b_4 = 1 - \max\{d_a, d_{c2}\}. \tag{3b}$$

In this way, the duty cycles of the entire CFC are obtained.

Switch mode (i)	Switches on (in B_1)	Duty cycle (a_i)	e_{12} (e_i)	i_{cfc1} (i_i)
1	S_{A1}, S_{C1}	a_1	0	0
2	S_{A1}, S_{D1}	a_2	u_c	i_{12}
3	S_{B1}, S_{C1}	a_3	$-u_c$	$-i_{12}$
4	S_{B1}, S_{D1}	a_4	0	0
Switch mode (j)	Switches on (in B_2)	Duty cycle (b_j)	e_{13} (e_j)	i_{cfc2} (i_j)
1	S_{A2}, S_{C2}	b_1	0	0
2	S_{A2}, S_{D2}	b_2	u_c	i_{13}
3	S_{B2}, S_{C2}	b_3	$-u_c$	$-i_{13}$
4	S_{B2}, S_{D2}	b_4	0	0

TABLE 2. Switch modes of bridge converters in the CFC

4. MATHEMATICAL MODEL OF THE WHOLE SYSTEM

4.1. Mathematical Model of the CFC

There are four switching modes for each bridge converter. By summarizing these four modes, the relationship between u_c and e_{12} can be expressed as follows:

$$e_{12} = \sum_{i=1}^{4} a_i\, e_i = (a_2 - a_3)\, u_c. \tag{4}$$

Similarly, the relationship between u_c and e_{13} is derived as

$$e_{13} = \sum_{j=1}^{4} b_j\, e_j = (b_2 - b_3)\, u_c. \tag{5}$$

By considering the charging and discharging through the capacitor within a switching cycle, the equation between u_c, i_{12}, and i_{13} can also be obtained:

$$C\frac{du_c}{dt} = \sum_{i=1}^{4} a_i\, i_i + \sum_{j=1}^{4} a_j\, i_j = (a_2 - a_3)\, i_{12} + (b_2 - b_3)\, i_{13}. \tag{6}$$

Equations (4)–(6) can be simplified to Eqs. (7)–(9) by substituting the expressions of duty cycles in Eqs. (2) and (3):

$$e_{12} = (d_a - d_{c1}) u_c, \tag{7}$$

$$e_{13} = (d_a - d_{c2})\, u_c, \tag{8}$$

$$C\frac{du_c}{dt} = (d_a - d_{c1})\, i_{12} + (d_a - d_{c2})\, i_{13}. \tag{9}$$

Equations (7)–(9) form the dynamic model of the CFC. Eqs. (7) and (8) indicate that the CFC is equivalent to a controlled voltage source e_{12} for branch 12 and a controlled voltage source e_{13} for branch 13, whereas the magnitude of e_{12} and e_{13} can be controlled through d_{c1} and d_{c2} independently. This proves that the CFC can operate independently in different branches

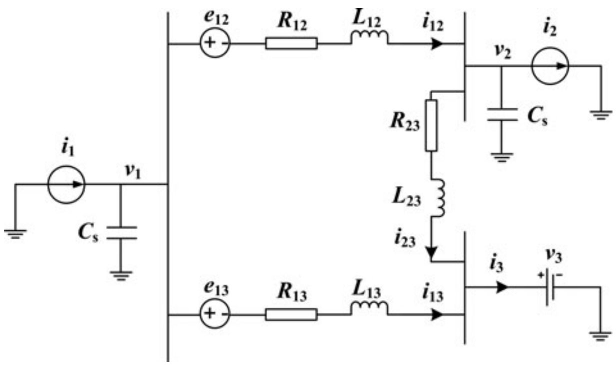

FIGURE 2. Equivalent representation of the whole system.

and has the potential to be implemented between two or more branches.

4.2. Equivalent Representation of the Whole System

The above analysis demonstrates that the CFC works as a controlled voltage source to the branches in which it is installed. An equivalent diagram of the whole system is given in Figure 2 with the following assumptions. First, for branches 12 and 13, as the CFC is equivalent to the controlled voltage sources, it is replaced by e_{12} in branch 12 and e_{13} in branch 13, respectively. Second, the focus of this article is the dynamics of the DC grid and the AC/DC converter dynamics are not considered. Therefore, both T_1 and T_2 are modeled by constant current sources, as these two terminals adopt constant power control. Meanwhile T_3 is modeled by a constant voltage source as it adopts constant voltage control. Third, the transmission lines are represented by a lumped proportional-integral (PI)-section model, a series combination of inductors and resistors with parallel capacitors. Fourth, during the calculations, the reactance of the DC side smoothing reactors (3 mH) is added into the values of the equivalent inductors of the DC transmission lines. Finally, the capacitances of the transmission line and that of the dual capacitor (2 μF) of the HVDC grid are combined at the outputs of T_1 and T_2, respectively. Based on these assumptions, the simplified equivalent diagram is shown in Figure 2.

4.3. Mathematical Model of the HVDC Network

To obtain systematic equations from Figure 2, both Kirchhoff's voltage law (KVL) and Kirchhoff's current law (KCL) are applied. First, three equations can be derived for branches 12, 13, and 23 based on the KVL theorem:

$$L_{12}\frac{di_{12}}{dt} + R_{12}i_{12} = v_1 - v_2 - e_{12}, \tag{10}$$

$$L_{13}\frac{di_{13}}{dt} + R_{13}i_{13} = v_1 - v_3 - e_{13}, \tag{11}$$

$$L_{23}\frac{di_{23}}{dt} + R_{23}i_{23} = v_2 - v_3. \tag{12}$$

Similarly, another two equations for T_1 and T_2 can be derived by using the KCL theorem:

$$C_s\frac{dv_1}{dt} = i_1 - i_{12} - i_{13}, \tag{13}$$

$$C_s\frac{dv_2}{dt} = i_{12} - i_{23} - i_2. \tag{14}$$

Equations (10)–(14) comprise the dynamic model of the HVDC network.

4.4. Mathematical Model of the Whole System

As the dynamic models for the HVDC network and the CFC are both obtained, a dynamic model for the whole system can be achieved by combining these two models. An overall dynamic model as shown in Eq. (15) is derived by combining Eqs. (7)–(9) and (10)–(14):

$$\dot{\mathbf{x}} = \mathbf{A}\mathbf{x} + \mathbf{B}\mathbf{v_{in}}, \tag{15a}$$

$$\mathbf{y} = \mathbf{C}\mathbf{x} + \mathbf{D}\mathbf{v_{in}}, \tag{15b}$$

where matrixes **A**, **B**, **C**, and **D** are shown in the Appendix, column vector **x** is the state vector, while $\mathbf{v_{in}}$ and **y** are the input vector and the output vector, respectively. They are defined as

$$\mathbf{x} = \begin{bmatrix} i_{12} \; i_{13} \; i_{23} \; v_1 \; v_2 \; u_c \end{bmatrix}^T,$$
$$\mathbf{v_{in}} = \begin{bmatrix} i_1 \; i_2 \; v_3 \end{bmatrix}^T, \quad \mathbf{y} = \begin{bmatrix} i_{12} \; u_c \end{bmatrix}^T.$$

The whole system is a three-input, two-output system. The three inputs are power dispatch and voltage regulation variables coming from three converter stations. The two outputs are variables to be regulated by the CFC. The variables and parameters in Eq. (15) have been labeled in Figure 1. In practice, duty cycles d_a and d_b can be set at any value as long as Eq. (1) is valid. In the following analysis, d_a and d_b are fixed at 0.5 to simplify the mathematical model.

4.4.1. Steady-state Model.

The steady-state model is obtained from Eq. (15) by setting the derivative vector $\dot{\mathbf{x}}$ to zero. Then the steady-state TF **G** can be achieved from the following equation:

$$\mathbf{G} = \mathbf{y}/\mathbf{v_{in}} = \mathbf{C}(-\mathbf{A}^{-1})\mathbf{B}, \tag{16a}$$

$$\begin{bmatrix} i_{12} \\ u_C \end{bmatrix} = \begin{bmatrix} -\dfrac{2*d_{c2}-1}{2*(d_{c1}-d_{c2})} & 0 & 0 \\ -\dfrac{3*d_{c1}+5*d_{c2}-4}{(d_{c1}-d_{c2})^2} & \dfrac{-4}{(d_{c1}-d_{c2})} & 0 \end{bmatrix} \times \begin{bmatrix} i_1 \\ i_2 \\ v_3 \end{bmatrix}. \tag{16b}$$

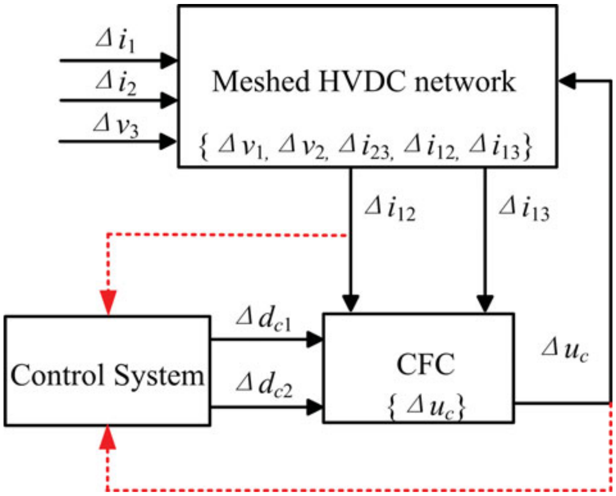

FIGURE 3. Small-signal relationship between the HVDC network and the CFC.

Using the parameters in Table 2, **G** is solved as a function of d_{c1} and d_{c2}, as shown in Eq. (16). Equation (16) shows that i_{12} is relevant to i_1, while u_c is dependent on both i_1 and i_2.

4.4.2. Small-signal Model

From Eq. (15), matrix $\mathbf{A_1}$ indicates that the system model becomes non-linear when either d_{c1} or d_{c2} is varying over time. The small-signal relationship between the HVDC network and the CFC is analyzed using two approaches.

First, the relationship is analyzed through a small-signal diagram. Figure 3 illustrates the small-signal relationship between the meshed HVDC network and the CFC. There are two different groups of signals in Figure 3: one is the state variables, which reflect the states of the HVDC network and the CFC; the other is the external signals, which have direct influence on the HVDC network or the CFC. In total there are six state variables, of which five variables are from the meshed HVDC network (Δi_{12}, Δi_{13}, Δi_{23}, Δv_1, Δv_2) and one is from the CFC (Δu_c). The DC network affects the CFC through Δi_{12} and Δi_{13}, while the CFC influences the DC network through Δu_c. Due to the influence of Δu_c, the power flow in the meshed DC grid can be controlled through the operation of the CFC.

In addition, the external signals also divide into two types. The first type consists of Δi_1, Δi_2, and Δv_3. They come from the external system of the DC network, such as the power dispatch and voltage regulation signals from converter stations. In the small-signal model, this type of signal is regarded as a disturbance input. The other type includes Δd_{c1} and Δd_{c2}, which come from the control system. They are the firing signals for the switches of the CFC. In the small-signal model, this type of signal is regarded as a control input. The focus of the control system design is to generate firing signals Δd_{c1} and Δd_{c2} from feedback signals Δi_{12} and Δu_c.

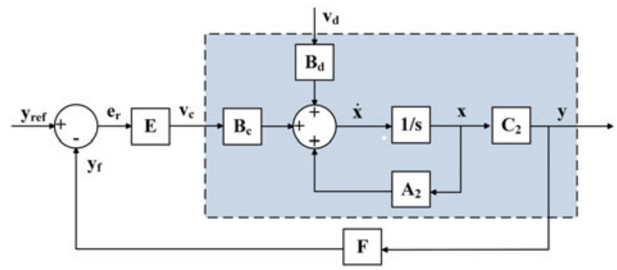

FIGURE 4. System transfer diagram based on the small-signal model.

In addition to using diagrams to describe the relationship, it can also be expressed by equations. The systematic small-signal equations are derived by applying small perturbations to Eq. (14). The result is

$$\Delta\dot{\mathbf{x}} = \mathbf{A_2}\Delta\mathbf{x} + \mathbf{B_c}\Delta\mathbf{v_c} + \mathbf{B_d}\Delta\mathbf{v_d}, \tag{17a}$$

$$\Delta\mathbf{y} = \mathbf{C_2}\Delta\mathbf{x}, \tag{17b}$$

where matrixes $\mathbf{A_2}$, $\mathbf{B_c}$, and $\mathbf{B_d}$ are shown in the Appendix, and small-signal vectors $\Delta\mathbf{x}$, $\Delta\mathbf{y}$, $\Delta\mathbf{v_c}$, and $\Delta\mathbf{v_d}$ are

$$\begin{aligned} \Delta\mathbf{x} &= \left[\Delta i_{12}\ \Delta i_{13}\ \Delta i_{23}\ \Delta v_1\ \Delta v_2\ \Delta u_c\right]^T, \\ \Delta\mathbf{y} &= \left[\Delta i_{12}\ \Delta u_c\right]^T, \\ \Delta\mathbf{v_c} &= \left[\Delta D_{c1}\ \Delta D_{c2}\right]^T, \Delta\mathbf{v_c} = \left[\Delta i_1\ \Delta i_2\ \Delta v_3\right]^T. \end{aligned}$$

In Eq. (17), matrices $\mathbf{A_2}$, $\mathbf{B_d}$, $\mathbf{B_c}$, and $\mathbf{C_2}$ are the state matrix, control input matrix, output matrix, and disturbance input matrix, respectively. In $\mathbf{A_2}$, D_{c1} and D_{c2} are the steady-state values of d_{c1} and d_{c2}, respectively. Based on matrix $\mathbf{A_2}$, system eigenvalues can be obtained. In $\mathbf{B_c}$, i_{12}, i_{13}, and u_c are the steady-state values of the current in branches 12 and 13 and the capacitor voltage of the CFC, respectively. There are two types of inputs, control input $\Delta\mathbf{v_c}$ and disturbance input $\Delta\mathbf{v_d}$. Two outputs are in the output vector $\Delta\mathbf{y}$. Feedback control is employed to ensure output tracking of the reference values. Detailed system analysis and control system design are presented in the next section.

Operating point	1	2
D_{c1}	0.068	0.625
D_{c2}	0.788	0.125
i_{12}	$0.8kA$	$1.5kA$
u_c	$5kV$	$4kV$

TABLE 3. Parameters of two critical steady-state operating points of the CFC

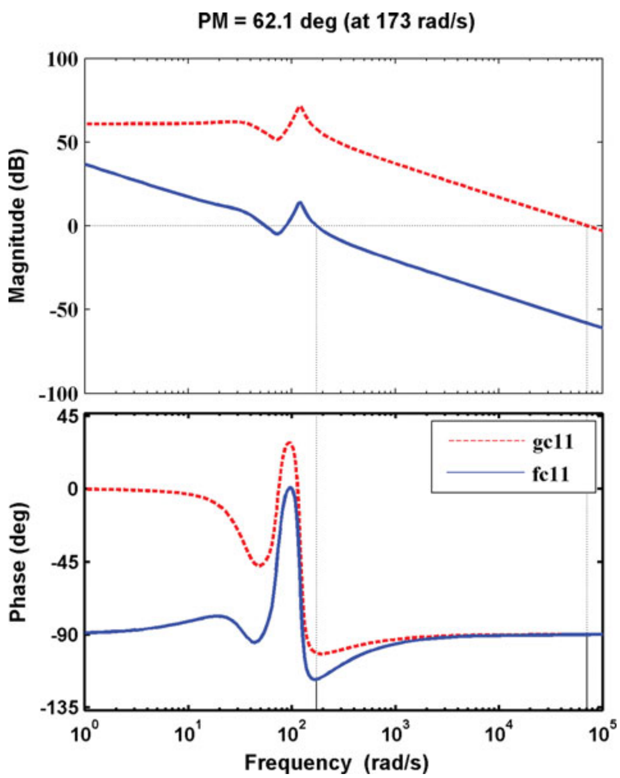

FIGURE 5. Bode diagrams of g_{c11} and f_{c11}.

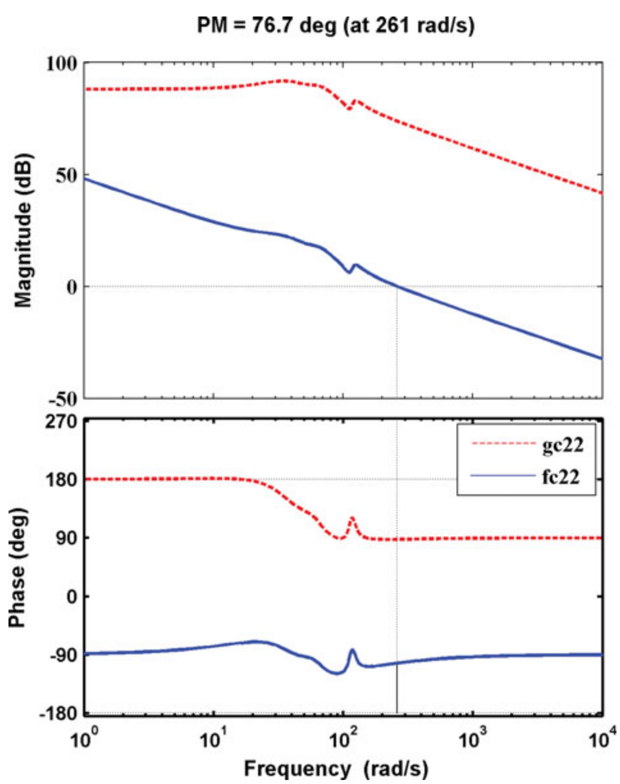

FIGURE 6. Bode diagrams of g_{c22} and f_{c22}.

Eigenvalues	Without matrix **E**	With matrix **E**
$\lambda_{1,2}$	$-20.005 \pm 54.158i$	$-21.443 \pm 52.565i$
$\lambda_{3,4}$	$-23.379 \pm 75.055i$	$-29.062 \pm 11.812i$
λ_5	$-71{,}439$	$-33.856 \pm 101.05i$
λ_6	$1.2e{+}006$	
$\lambda_{7,8}$		$-124.09 \pm 123.29i$

TABLE 4. Eigenvalue comparisons of the system with/without matrix **E**

An eigenvalue's real and imaginary parts are shown in 1/sec and rad/sec.

5. SMALL-SIGNAL ANALYSIS

The analysis of the small-signal model and the design of suitable controllers can be conducted by using a few methods, such as Block diagram, Bode plot, and root locus. First, a block diagram is drawn in Figure 4 based on the relationships in Eq. (17). In Figure 4, $\mathbf{B_c}$, $\mathbf{B_d}$, $\mathbf{A_2}$, and $\mathbf{C_2}$ are the system matrices in Eq. (17), while $\dot{\mathbf{x}}$ is a vector made up of the derivatives of state vector $\mathbf{x}$. In Figure 4, the open-loop system is indicated by the gray area, which illustrates two control loops from disturbance input vector $\boldsymbol{v_d}$ and control input vector $\boldsymbol{v_c}$ to output vector $\boldsymbol{y}$. Then $\boldsymbol{y}$ is fed back through matrix $\mathbf{F}$, and $\boldsymbol{y_f}$ is compared with reference value $\boldsymbol{y_{ref}}$. The result of comparison

Quantity of AC grid	Value	Quantity of DC grid	Value
Nominal AC source voltage	239 kV	MMC rated capacity	640 MVA
L_{AC}	150 mH	Nominal DC voltage	±160 kV
Nominal AC frequency	50 Hz	Branch 12 cable resistance R_{12}	1 Ω
Transformer voltage ratio	239/155 kV (Y/Δ)	Branch 13 cable resistance R_{13}	3 Ω
Transformer rating	750 MVA	Branch 23 cable resistance R_{23}	4 Ω
Transformer leakage inductance	5%	Branch 12 cable inductance L_{12}	0.07 H
R	0.03 Ω	Branch 13 cable inductance L_{13}	0.09 H
L	0.0153H	Branch 23 cable inductance L_{23}	0.10 H
Submodule capacitor	2500 μF	Equivalent capacitor C_s	$3e$–3 F
		CFC capacitor C_{cfc}	$2e$–3 F

TABLE 5. Parameters of the meshed 3-T MMC-HVDC system

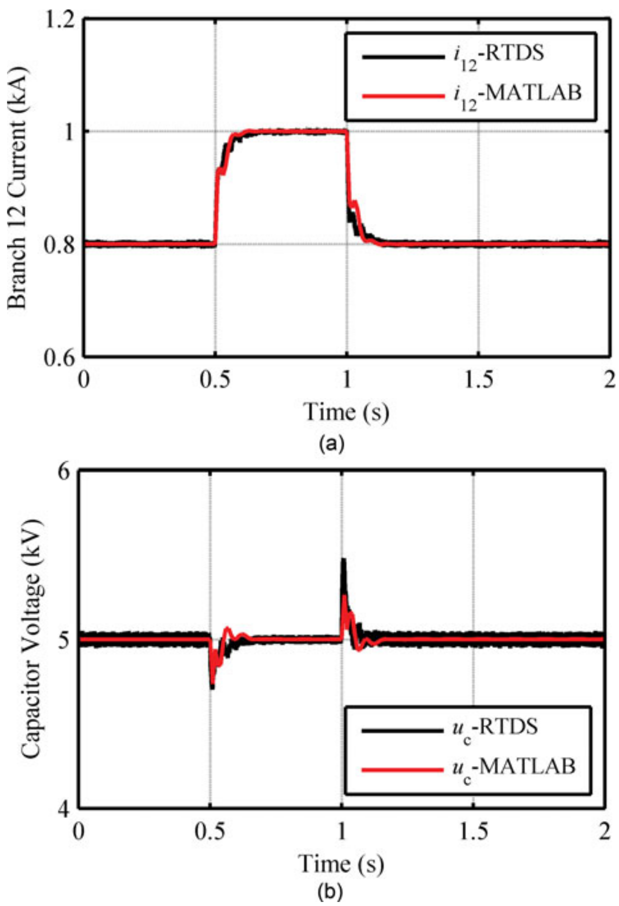

FIGURE 7. System dynamic response to a step change of i_{12ref}.

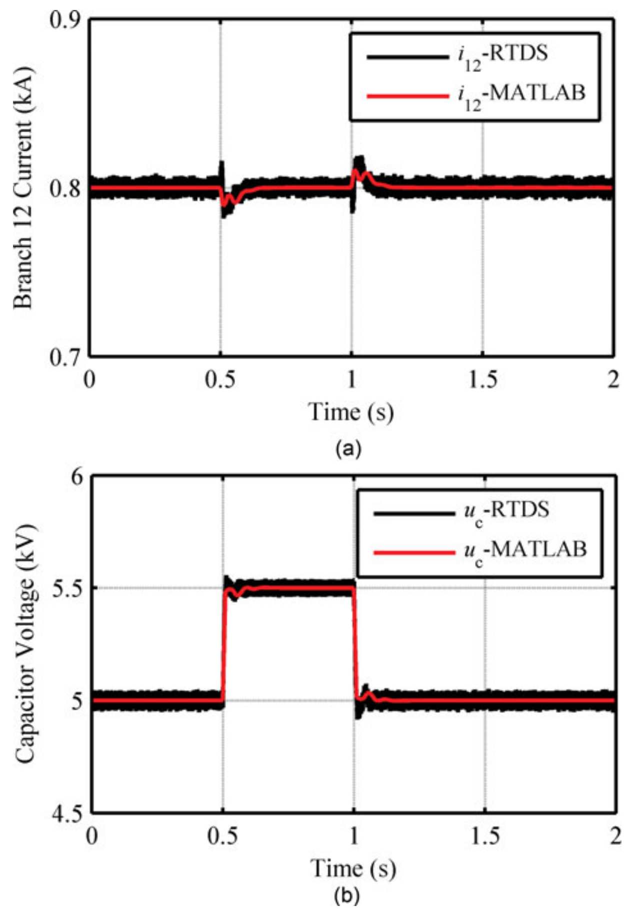

FIGURE 8. System dynamic response to a step change of u_{cref}.

$\mathbf{e_r}$ passes through control matrix $\mathbf{E}$ so that $\boldsymbol{v_c}$ is obtained. In the next few sections, the open-loop system, control matrix design, and feedback system will be described.

5.1. Open-loop System

From Figure 4, the relationship of the open-loop system is expressed as follows:

$$\dot{\mathbf{x}} = \mathbf{A_2 x} + \mathbf{B_c v_c} + \mathbf{B_d v_d}, \tag{18a}$$

$$\mathbf{y} = \mathbf{C_2 x}. \tag{18b}$$

From Eq. (17), the small-signal open loop TF $\mathbf{G_c}$ from $\mathbf{v_c}$ to $\mathbf{y}$ can be obtained, which is a 2-by-2 matrix:

$$\mathbf{y} = \mathbf{G_c v_c}, \tag{19}$$

where

$$\mathbf{G_c} = \begin{bmatrix} g_{c11} & g_{c12} \\ g_{c21} & g_{c22} \end{bmatrix}.$$

In addition, the open-loop TF $\mathbf{F_c}$ from vector $\mathbf{e_r}$ to $\mathbf{y}$ can also be expressed as

$$\mathbf{y} = \mathbf{F_c e_r} = \mathbf{F_c E^{-1} v_c}, \tag{20}$$

where

$$\mathbf{F_c} = \begin{bmatrix} f_{c11} & f_{c12} \\ f_{c21} & f_{c22} \end{bmatrix}, \quad \mathbf{e_r} = \begin{bmatrix} i_{12ref} - i_{12} \\ u_{cref} - u_c \end{bmatrix}.$$

As $\mathbf{G_c}$ and $\mathbf{F_c}$ are obtained, comparisons can be made between the two TFs to analyze the performance of control matrix $\mathbf{E}$.

5.2. Control System Design

Before the design of the control system, the steady-state operating point of the CFC should be determined first. In this article, the operating range of i_{12} is between 0.8 and 1.5 kA, while u_c is between 4 and 5 kV. Table 3 shows the results for two critical operating points after solving steady-state TFs in Eq. (16). The next stage is to design the control system to make the CFC operate satisfactorily in the whole operating range.

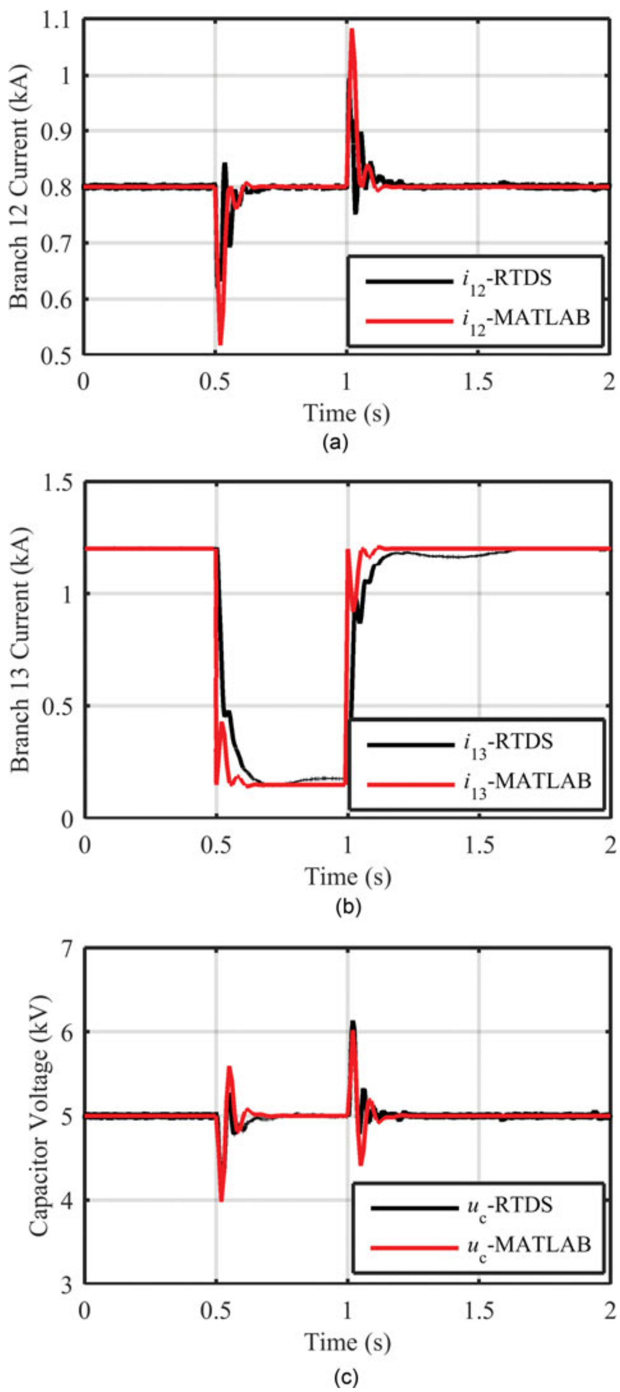

FIGURE 9. System dynamic response to the disturbance of i_1.

The control system is designed under the following performance objectives. First, under steady state, output $\mathbf{y}$ should be able to track reference value $\mathbf{y_{ref}}$. Second, the small-signal stability of the system needs to be satisfied. Third, the phase margin (PM) of $\mathbf{F_c}$ should be larger than 60° to achieve an

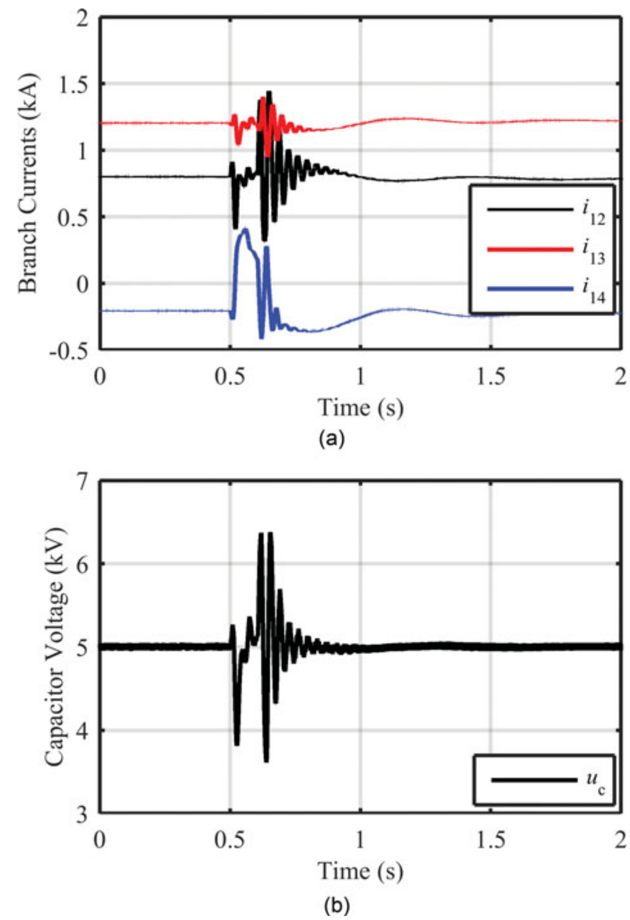

FIGURE 10. System dynamic response to AC fault at T_2 (with CFC).

acceptable dynamic response. Finally, the influence of disturbances should be minimized.

As stated in the first objective, $\mathbf{y}$ needs to track $\mathbf{y_{ref}}$; therefore, two PI controllers are adopted in control system $\mathbf{E}$. The

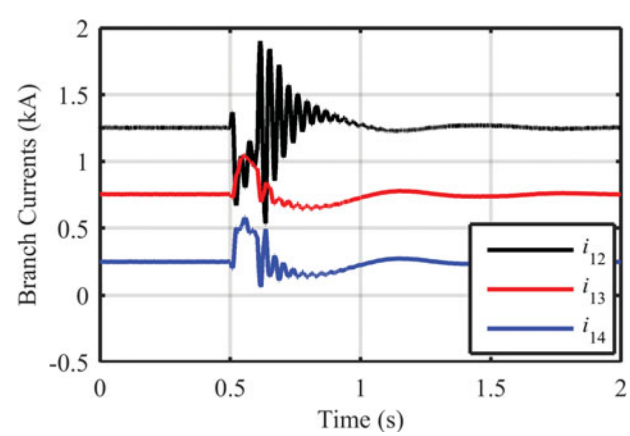

FIGURE 11. System dynamic response to AC fault at T_2 (without CFC).

expression of matrix **E** is shown below:

$$\mathbf{E} = \begin{bmatrix} \dfrac{PI_1}{i_{12ref}} & 0 \\ 0 & \dfrac{PI_2}{u_{cref}} \end{bmatrix} = \begin{bmatrix} \dfrac{K_{P1}+K_{I1}/s}{i_{12ref}} & 0 \\ 0 & \dfrac{-(K_{P2}+K_{I2}/s)}{u_{cref}} \end{bmatrix}, \tag{21}$$

where K_{P1}, K_{I1}, K_{P2}, and K_{I2} are parameters of PI_1 and PI_2. Control objectives are reached by selecting suitable parameters for matrix **E** based on the analysis of TF $\mathbf{F_c}$.

5.3. Control System Performance Analysis

To evaluate the effectiveness of the control systems, both Bode diagram and root locus are adopted. The following analysis is based on operating point 1 in Table 3.

Figure 5 shows the Bode diagram of the open-loop TFs g_{c11} (from d_{c1} to i_{12}) and f_{c11} (from i_{12ref}–i_{12} to i_{12}). Meanwhile Figure 6 shows the Bode diagram of g_{c22} (from d_{c2} to u_c) and f_{c22} (from u_{cref}–u_c to u_c).

From Figures 5 and 6, it can be found that the gains of f_{c11} and f_{c22} have largely been alleviated by PI controllers compared with g_{c11} and g_{c22}. In the low-frequency range, f_{c11} and f_{c22} have a –20 dB/decade decrease as PIs introduce a pole at the origin of the s-plane. In Figure 6, the PM of g_{c22} is –90° ($\omega_{gc} = 1.2e6$ rad/s). This negative PM can lead to the instability of the closed-loop system. However, compared with the negative margin of g_{c22}, the PM of f_{c22} has largely been improved. This is due to PI_2, which has a minus sign in Eq. (21) to create a 180° phase shift. After the compensation, the PM of f_{c11} and f_{c22} is 62.1° ($\omega_{gc} = 173$ rad/s) and 76.7° ($\omega_{gc} = 261$ rad/s), respectively, which can greatly improve the dynamic performance of the closed-loop system.

5.4. Closed-loop System

As shown in Figure 4, the system becomes a closed loop by subtracting $\mathbf{y_f}$ from $\mathbf{y_{ref}}$. Therefore, the closed-loop state-space system can be written as in Eq. (22):

$$\dot{\mathbf{x}} = \mathbf{A_2x} + \mathbf{B_cE}\,(\mathbf{y_{ref}} - \mathbf{FCx}) + \mathbf{B_d u_d}, \tag{22a}$$

$$\mathbf{y} = \mathbf{C_2x}, \tag{22b}$$

where feedback matrix **F** is a 2-by-2 unit matrix. Based on Eq. (22), the closed-loop TF $\mathbf{G_{c\_cl}}$ between $\mathbf{y_{ref}}$ and **y** can be obtained. Similarly, the sensitivity function $\mathbf{G_{d\_cl}}$ from $\mathbf{v_d}$ to **y** is also derived. Whether **y** can track $\mathbf{y_{ref}}$ effectively can be examined by the steady-state value of $\mathbf{G_{c\_cl}}$. Similarly, the steady-state value of $\mathbf{G_{d\_cl}}$ is set to zero to minimize the impact of the disturbances $\mathbf{v_d}$ to output **y**. The eigenvalues of the system with/without matrix E are summarized and compared in Table 4, which indicates the stability of the whole system is improved due to the functionality of the control system.

6. SIMULATION RESULTS

The meshed 3-T MMC HVDC simulation system shown in Figure 1 was built via an RTDS to validate the effectiveness of the theoretical analysis and the control system. The system parameters are shown in Table 5. The simulation platform used is RSCAD, which is the software associated with the RTDS hardware (RTDS Technologies, Inc., Winnipeg, MB, Canada).

6.1. Case 1: System Response to a Step Change of $\mathbf{i_{12ref}}$

Initially, i_{12ref} was set to 0.8 kA. At $t = 0.5$ sec, i_{12ref} increased to 1 kA and then recovered to the initial value at 1 sec. Figures 7(a) and 7(b) shows the responses of i_{12} and u_c, respectively, with comparisons made between the results from the RTDS simulation model and the theoretical model, which is the system mathematical model established in MATLAB. During this transient response, i_{12} tracked the new reference value in a short transitional time and with acceptable overshoot. Meanwhile u_c also experienced a transient fluctuation while its steady-state value was not affected. It can also be observed that the results from the simulation model match with the results from the theoretical model; this shows the validity of the theoretical modeling and the effectiveness of the designed proportional-integral-differential (PID) controllers.

6.2. Case 2: System Response to Step Change of $\mathbf{u_{cref}}$

In Case 2, the step change of u_{cref} is analyzed. As shown in Figures 8(a) and 8(b), u_c was originally set to 5 kV and i_{12} was set to 0.8 kA. At 0.5 sec, as u_{cref} reduced to 4.5 kV, u_c tracked the change of u_{cref} within 0.2 sec with negligible overshoot. Meanwhile, i_{12} experienced a positive overshoot as the common capacitor of the CFC discharged to bBranch 12. Conversely, i_{12} experienced a negative overshoot when u_{cref} recovered back to 5 kV since branch 12 charged the CFC during the transient.

6.3. Case 3: System Response to the Disturbance of the Active Cower at $\mathbf{T_1}$

In this case, when the active power at T_1, P_1, decreased suddenly, this disturbance was accommodated by branch 13, as in branch 12, i_{12} was regulated to a fixed value by the CFC. Figures 9(a), 9(b), and 9(c) show the dynamic response of i_{12}, i_{13}, and u_c after a disturbance of P_1. In addition, as the small-signal model is based on the linearization around a particular operation point, during large disturbances, the results from the small-signal model may be slightly different from the results of the non-linear simulation model. It can be observed in Figure 9 that the difference between the RTDS model and the MATLAB model is increased compared to the differences in Cases 1 and 2.

6.4. Case 4: System Response to AC Fault at T_2

Figures 10 and 11 present the system responses to an AC short-circuit fault at T_2 ($R_s = 1\ \Omega$, $t_s = 100$ ms) with/without CFC. It can be seen that the CFC with the designed control parameters can ride through large disturbances and function normally. The branch currents of the 3-T system with the assistance of the CFC experienced smaller transient over-currents compared with the system without a CFC, which can be seen from the transients of i_{12}.

7. CONCLUSIONS

The main contribution of this article is the establishment of a small-signal model of a 3-T meshed DC grid including a DC CFC and the design of parameters for the control system of the CFC. A control system that satisfies both stability and dynamic performance requirements has been designed based on the established small-signal models. The validity of the theoretical modeling has been verified through comparisons with the results from the RTDS simulation model, and the effectiveness of the control system has been demonstrated via various cases. This article has laid the theoretical foundation for potential applications of the CFC. The impact of the MMC dynamics and AC network dynamics on the small-signal modeling of the DC grid will be investigated in future research.

REFERENCES

[1] Xu, L., Yao, L., and Christian, S., "Grid integration of large DFIG-based wind farms using VSC transmission," *IEEE Trans. Power Syst.*, Vol. 22, No. 3, pp. 976–984, August 2007.

[2] Lu, W., and Ooi, B.-T., "Premium quality power park based on multi-terminal HVDC," *IEEE Trans. Power Del.*, Vol. 20, No. 2, pp. 978–983, April 2005.

[3] Lu, W., and Ooi, B.-T., "Optimal acquisition and aggregation of offshore wind power by multiterminal voltage-source HVDC," *IEEE Trans. Power Del.*, Vol. 18, No. 8, pp. 201–206, January 2003.

[4] Daelemans, G., Srivastava, K., Reza, M., Cole, S., and Belmans, R., "Minimization of steady-state losses in meshed networks using VSC HVDC," *IEEE Power & Energy Society General Meeting*, pp. 1–5, Calgary, AB, 26–30 July 2009.

[5] Xu, L., and Yao, L., "DC voltage control and power dispatch of a multi-terminal HVDC system for integrating large offshore wind farms," *IET Renew. Power Gener.*, Vol. 5, No. 3, pp. 223–233, May 2011.

[6] Akhmatov, V., Callavik, M., Franck, C. M., Rye, S. E., Ahndorf, T., Bucher, M. K., Muller, H., Schettler, F., and Wiget, R., "Technical guidelines and prestandardization work for first HVDC grids," *IEEE Trans. Power Del.*, Vol. 29, No.1, pp. 327–335, February 2014.

[7] Pan, J., Nuqui, R., Srivastava, K., Jonsson, T., Holmberg, P., and Hafner, Y. J., "AC grid with embedded VSC-HVDC for secure and efficient power delivery," *IEEE Energy 2030 Conference*, pp. 1–6, Atlanta, GA, 17–18 November 2008.

[8] Hiorns, A., Smith, R., and Wright, D., "An integrated approach to offshore electricity transmission," *9th IET International Conference on AC and DC Power Transmission*, pp. 1–5, London, UK, 19–21 October 2010.

[9] Huertas-Hernando, D., Svendsen, H. G., Warland, L., Troötscher, T., and Korpas, M., "Analysis of grid alternatives for north sea offshore wind farms using a flow-based market model," *7th International Conference on the European Energy Market (EEM)*, pp. 1–6, Madrid, Spain, 23–25 June 2010.

[10] Farahmand, H., Huertas-Hernando, D., Warland, L., Korpas, M., and Svendsen, H. G., "Impact of system power losses on the value of an offshore grid for north sea offshore wind," *IEEE PowerTech*, pp. 1–7, Trondheim, Norway, 19–23 June 2011.

[11] Jovcic, D., Hajian, M., Zhang, H., and Asplund, G., "Power flow control in DC transmission grids using mechanical and semiconductor based DC/DC devices," *10th IET International Conference on AC and DC Power Transmission*, pp. 1–6, London, UK, 19–21 October 2010.

[12] Mu, Q., Liang, J., Li, Y., and Zhou, X., "Power flow control devices in DC grids," *IEEE Power and Energy Society General Meeting*, pp. 1–7, San Diego, CA, 22–26 July 2012.

[13] Kish, G. J., and Lehn, P. W., "A modular bidirectional DC power flow controller with fault blocking capability for DC networks," *Proceedings of the IEEE 14th Workshop on Control Modeling Power Electronics*, pp. 1–7, Salt Lake City, UT, 23–26 June 2013.

[14] Kish, G. J., Ranjram, M., and Lehn, P. W., "A modular multilevel DC/DC converter with fault blocking capability for HVDC interconnects," *IEEE Trans. Power Electron.*, Vol. 30, No. 1, pp. 148–162, January 2015.

[15] Veilleux, E., and Ooi, B. T., "Multi-terminal HVDC with thyristor power-flow controller," *IEEE Trans. Power Del.*, Vol. 27, No. 3, pp. 1205–1212, 2012.

[16] Kumar, B., Subhasish, M., Tomas, J., and Sasitharan, S., "Series-connected DC/DC converter for controlling the power flow in a HVDC power transmission system," PCT WO 2012/037964A1, 2012.

[17] Dimitris, G., Soubhik, A., Mats, H., Mukherjee, S., Tomas, J., Bopparaju, G., and Carl, H., "An arrangement for controlling the electric power transmission in a HVDC power transmission system," PCT WO 2013/091700A1, 2013.

[18] Zhang, T., Li, C., and Liang, J., "A thyristor based series power flow control device for multi-terminal HVDC transmission," *49th International Universities Power Engineering Conference (UPEC)*, pp. 1–5, Cluj-Napoca, Romania, 2–5 September 2014.

[19] Balasubramaniam, S., Liang, J., and Ugalde-Loo, C. E., "An IGBT based series power flow controller for multi-terminal HVDC transmission," *49th International Universities Power Engineering Conference (UPEC)*, pp. 1–6, Cluj-Napoca, Romania, 2–5 September 2014.

[20] Xu, F., and Xu, Z., "A modular multilevel power flow controller for meshed HVDC grids," *Sci. China Tech. Sci.*, Vol. 57, No. 9, pp. 1773–1784, September 2014.

[21] Chen, W., Zhu, X., Yao, L., Ruan, X., Wang, Z., and Cao, Y., "An interline DC power flow controller (IDCPFC) for multi-terminal HVDC system," *IEEE Trans. Power Del.*, Vol. 30, No. 4, pp. 2027–2036, 2015.

[22] Barker, C. D., and Whitehouse, R. S., "A current flow controller for use in HVDC grids," in *IET 10th International Conference*

on AC and DC Power Transmission, pp. 1–5, London, UK, 19–21 October 2012.

[23] Deng, N., Wang, P., Zhang, X.-P., Tang, G. F., and Cao, J. Z., “A DC current flow controller for meshed modular multilevel converter multiterminal HVDC grids”, *CSEE J. Power Energy Syst.*, Vol. 1, No. 1, pp. 43–51, March 2015.

[24] Zhang, X.-P., Rehtanz, C., and Pal, B., “FACTS-devices and applications,” in *Flexible AC Transmission Systems: Modelling and Control*, Berlin: Springer, Chap. 1, pp. 15–26, 2006.

[25] Zhang, X.-P., “Multiterminal voltage-sourced converter-based HVDC models for power flow analysis,” *IEEE Trans. Power Syst.*, Vol. 19, pp. 1877–1884, 2004.

APPENDIX

$$\mathbf{A} = \begin{bmatrix} \frac{-R_{12}}{L_{12}} & 0 & 0 & \frac{1}{L_{12}} & \frac{-1}{L_{12}} & \frac{-(d_{c1}-0.5)}{L_{12}} \\ 0 & \frac{-R_{13}}{L_{13}} & 0 & \frac{1}{L_{13}} & 0 & \frac{-(d_{c2}-0.5)}{L_{13}} \\ 0 & 0 & \frac{-R_{23}}{L_{23}} & 0 & \frac{1}{L_{23}} & 0 \\ \frac{-1}{C_s} & \frac{-1}{C_s} & 0 & 0 & 0 & 0 \\ \frac{1}{C_s} & 0 & \frac{-1}{C_s} & 0 & 0 & 0 \\ \frac{(0.5-d_{c1})}{C_{cfc}} & \frac{(0.5-d_{c2})}{C_{cfc}} & 0 & 0 & 0 & 0 \end{bmatrix},$$

$$\mathbf{B} = \begin{bmatrix} 0 & 0 & 0 & \frac{1}{C_s} & 0 & 0 \\ 0 & 0 & 0 & 0 & \frac{-1}{C_s} & 0 \\ 0 & \frac{-1}{L_{13}} & \frac{-1}{L_{23}} & 0 & 0 & 0 \end{bmatrix}^T,$$

$$\mathbf{C} = \begin{bmatrix} 1 & 0 & 0 & 0 & 0 & 0 \\ 0 & 0 & 0 & 0 & 0 & 1 \end{bmatrix}, \quad \mathbf{D} = \begin{bmatrix} 0 & 0 & 0 \\ 0 & 0 & 0 \end{bmatrix},$$

$$\mathbf{A_2} = \begin{bmatrix} \frac{-R_{12}}{L_{12}} & 0 & 0 & \frac{1}{L_{12}} & \frac{-1}{L_{12}} & \frac{(D_{c1}-0.5)}{L_{12}} \\ 0 & \frac{-R_{13}}{L_{13}} & 0 & \frac{1}{L_{13}} & 0 & \frac{(D_{c2}-0.5)}{L_{13}} \\ 0 & 0 & \frac{-R_{23}}{L_{23}} & 0 & \frac{1}{L_{23}} & 0 \\ \frac{-1}{C_s} & \frac{-1}{C_s} & 0 & 0 & 0 & 0 \\ \frac{1}{C} & 0 & \frac{-1}{C_s} & 0 & 0 & 0 \\ \frac{(0.5-D_{c1})}{C_{cfc}} & \frac{(0.5-D_{c2})}{C_{cfc}} & 0 & 0 & 0 & 0 \end{bmatrix},$$

$$\mathbf{B_d} = \begin{bmatrix} 0 & 0 & 0 & \frac{1}{C_s} & 0 & 0 \\ 0 & 0 & 0 & 0 & \frac{-1}{C_s} & 0 \\ 0 & \frac{-1}{L_{13}} & \frac{-1}{L_{23}} & 0 & 0 & 0 \end{bmatrix}^T,$$

$$\mathbf{B_c} = \begin{bmatrix} \frac{u_C}{L_{12}} & 0 & 0 & 0 & 0 & \frac{-i_{12}}{C_s} \\ 0 & \frac{u_C}{L_{13}} & 0 & 0 & 0 & \frac{-i_{13}}{C_s} \end{bmatrix}^T, \mathbf{C_2} = \begin{bmatrix} 1 & 0 & 0 & 0 & 0 & 0 \\ 0 & 0 & 0 & 0 & 0 & 1 \end{bmatrix}.$$

BIOGRAPHIES

Na Deng received her B.Eng. from Huazhong University of Science and Technology (HUST), China, in 2011 and her Ph.D. from University of Birmingham, Birmingham, UK, in 2015. She is currently an engineer in ABB Sifang Power System Co., China. Her research interests are the applications of DC/DC and AC/DC converters in HVDC systems and microgrids.

Puyu Wang received his B.Eng. from HUST, China, and University of Birmingham, Birmingham, UK, in electrical engineering in 2011 and his Ph.D. from University of Birmingham, Birmingham, UK, in 2016. He has been a research fellow with University of Birmingham, Birmingham, UK, since 2013. His research interests include VSC-HVDC technology, DC-DC converters, grid integration of renewable energy, and power electronics applications in power systems.

Xiao-Ping Zhang received his B.Eng., M.Sc., and Ph.D. in electrical engineering from Southeast University, China, in 1988, 1990, 1993, respectively. He is currently a professor in electrical power systems at University of Birmingham, Birmingham, UK, and director of the smart grid of Birmingham Energy Institute. Before joining University of Birmingham, he was an associate professor in the School of Engineering at University of Warwick, Coventry, UK. From 1998 to 1999, he was visiting University of Manchester Institute of Science and Technology (UMIST). From 1999 to 2000, he was an Alexander Von Humboldt Research Fellow with University of Dortmund, Germany. He worked at China State Grid Electric Power Research Institute (EPRI) on Energy Management System (EMS)/Distribution Management System (DMS) advanced application software research and development between 1993 and 1998. He is co-author of the monograph *Flexible AC Transmission Systems: Modelling and Control* (New York: Springer, 2006 and 2012) and the book *Restructured Electric Power Systems: Analysis of Electricity Markets with Equilibrium Models* (Hoboken, NJ: Wiley/IEEE, 2010). He pioneered the concepts of global power and energy internet, energy union, and the UK’s energy valley. His research interests include smart grids, HVDC, FACTS, power system operation, control and protection, grid application of energy storage, energy market modeling, and management of distributed energy sources (including electrical vehicles (EVs), photo-voltaics (PVs) wind turbines, etc.) and systems.